ACS Energy LETTERS

http://pubs.acs.org/journal/aelccp

Hydroxyl Functional Groups in Two-Dimensional Dion–Jacobson Perovskite Solar Cells

Bat-El Cohen, Tal Binyamin, Tzipora Ben-Tzvi, Oren Goldberg, Adi Schlesinger, Isaac Balberg, Oded Millo, Elad Gross, Doron Azulay, and Lioz Etgar*

Cite This: *ACS Energy Lett.* 2022, 7, 217–225

Read Online

ACCESS | Metrics & More | Article Recommendations | Supporting Information

ABSTRACT: **In this work we demonstrate a new diammonium spacer molecule with hydroxyl functional groups forming a Dion–Jacobson perovskite. Polarization modulation infrared reflection absorption spectroscopy reveal hydrogen bonding between the iodide to the spacer molecule and in between the OH groups. As a result, we were able to demonstrate n = 5 low dimensional perovskite solar cell (LDPSC) with an efficiency of 10%. Photoconductivity measurements and scanning tunneling spectroscopy draw the band structure of this low dimensional perovskite (LDP) revealing in-gap states adjacent to the conduction band edge, consistent with Shockley–Reed–Hall modeling of the temperature-dependent photoconductivity. The LDPSC based on the diammonium spacer $H_3N–C_4H_6(OH)_2–NH_3$ shows enhanced stability under a relative humidity of more than 50% over 1030 h. Evaluating the mechanism of the cell shows a misalignment of the hole selective contact with the LDP. Improving this interface can increase further the photovoltaic performance, demonstrating the potential of this new type of diammonium spacer in LDP.**

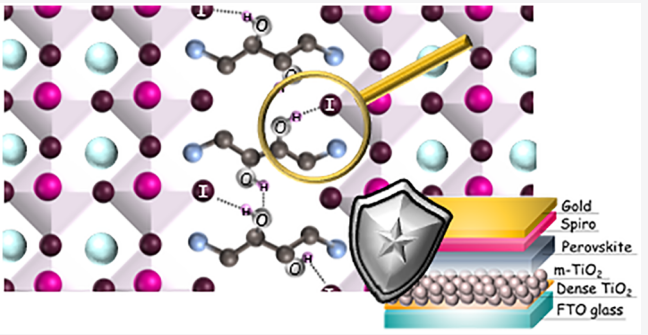

In recent years, two-dimensional (2D) perovskites attracted lot of attention as a promising material to be used in perovskite solar cells (PSCs). The ability to combine low dimensional perovskite in solar cells enhances the stability of the cell, enables tuning the band gap of the perovskite, and widens the range of possible light harvester in the solar-cell.

The structure of the 2D perovskite is composed of a metal halide framework and a long organic cation that acts as a barrier molecule between the inorganic sheets. It may also contain a small organic cation that fits in its size to the octahedra hole (forming in between the metal–halide) and form a complex structure of confined AMX_3 sheets (where A is a small organic cation according to Goldschmidt tolerance factor,[1] M is a 6 coordinate divalent metal, and X is a halide) in between the long organic molecules.[2,3] The perovskite can be modified according to the stoichiometric amount of the precursors based on the chemical formula $(R–NH_3)_2(A)_{n-1}(M)_n(X)_{3n+1}$ for monoammonium spacer or $(H_3N–R–NH_3)(A)_{n-1}(M)_n(X)_{3n+1}$ for a diammonium spacer. Most of the reports on a low-dimensional perovskite concentrate on monoammonium spacers that form the Ruddlesden–Popper 2D phase.[4−6] The implementation of low-dimensional perovskite in PSCs is challenging; the long organic molecules form a barrier for the carrier to flow in the cell and thus decrease the cell performance.[4,7−9] One way to combine these molecules in solar cells is to use a very small amount of them in the perovskite solution, which keeps the good photoconductivity characters of the 3D perovskite while increasing the stability and in some cases improving the cell performance.[4,10−13] However, this approach has a relatively small effect on the stability due to the small amount of the barrier molecule. Another way is to use a high amount of barrier molecules, but in this case the barrier molecules need to be arranged in a way that enables free pathways for the carriers through the perovskite toward the selective contacts.[14−16] The latter is the favorable way to increase the perovskite performance and to observe better resistivity to humidity. There are two main methods that assist in improving the cell

Received: September 14, 2021
Accepted: November 29, 2021

https://doi.org/10.1021/acsenergylett.1c01990
ACS Energy Lett. 2022, 7, 217–225

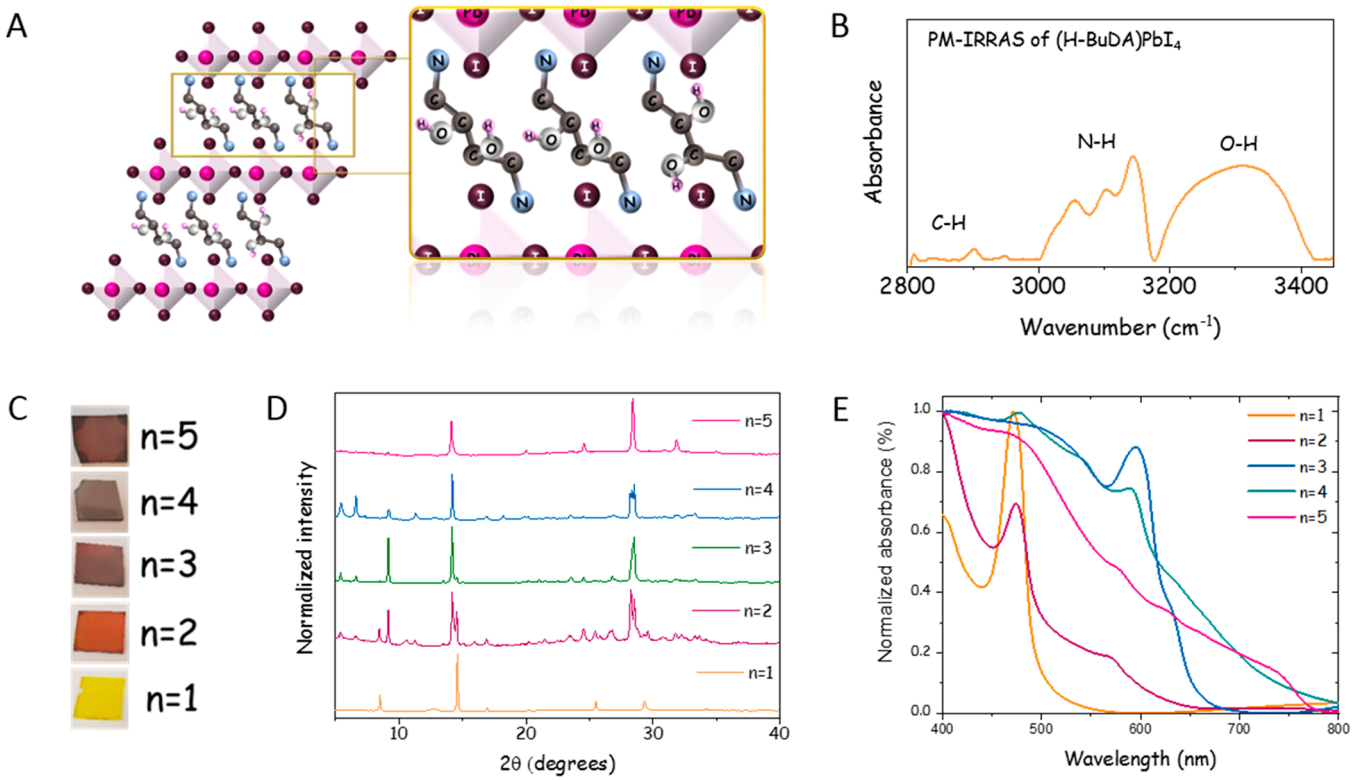

Figure 1. (A) Schematic illustration of the attachment of H-BuDA spacer for the perovskite inorganic framework MX_4^{2-}. The blow-up on the right shows the possible intermolecular hydrogen bond. (B) PM-IRRAS shows the aliphatic C−H stretch (2902 and 2946 cm^{-1}), broader N−H stretch (3000−3150 cm^{-1}, with noticeable peaks at 3054, 3103, and 3144 cm^{-1}), and intermolecular hydrogen bonded O−H stretch (3150−3450 cm^{-1}) of (H-BuDA)PbI_4 perovskite on TiO_2 substrate. The full spectrum can be seen in Figure S4B. (C) (H-BuDA)$(MA)_{n-1}Pb_nI_{3n+1}$ layered perovskite films (n = 1−5). (D) and (E) X-ray diffraction and absorbance spectra of layered perovskite films for (H-BuDA)$(MA)_{n-1}Pb_nI_{3n+1}$ (n = 1−4) and (H-BuDA)$(Cs_{0.20}MA_{0.13}FA_{0.67})_4Pb_5(I_{0.9}Br_{0.1})_{16}$ (n = 5), respectively. (The PL spectrum is observed in Figure S5.)

performance when using significant amount of barrier molecules (i.e., low dimensional perovskite): (i) special deposition techniques such as hot casting and (ii) chemical modifications of the barrier molecules. The hot-casting technique for 2D perovskite was reported by Tsai et al., which showed for the first time a significant improvement in the photovoltaic (PV) performance of the cell while using low n values.[16] However, this technique is suitable only for planar architectures. In our previous work, we reported on 1,4-benzenedimethanamonium as a spacer molecule in low-dimensional Dion−Jacobson perovskite, demonstrating high PV performance without any special deposition techniques or additives.[15]

Two-dimensional perovskite based on diammonium barrier results with a stronger and tighter bond of the perovskite sheets (due to the replacement of the static interactions by hydrogen bonds),[17,18] less complexity of the system, and a shorter space between the inorganic sheets, which probably assist to create a more organized 2D structure. Herein, we report on a new type of diammonium spacer $H_3N-C_4H_6(OH)_2-NH_3$ (H-BuDA) having hydroxyl functional groups that can form intermolecular hydrogen bonds. These hydrogen bonds should increase the interactions between the inorganic sheets and reduce the entropy of the system. The use of hydroxyl functional groups can also improve the orientation of the perovskite sheets toward the TiO_2 substrate similar to carboxylic group ligands.[19,20] We studied the attachment of the H-BuDA barrier molecules to the PbI_4^{2-} framework, together with the inter and intra molecular interactions by X-ray diffraction (XRD) and infrared (IR) vibrations. Furthermore, the optical, structural, and photoconductivity properties of (H-BuDA)$(A)_{n-1}(M)_n(X)_{3n+1}$ perovskite films were characterized. Scanning tunneling microscopy (STM) and spectroscopy (STS), photocurrent spectroscopy, and temperature-dependent photoconductivity along with Shockley−Reed−Hall simulations were used to analyze the perovskite bandgap and in-gap defect states. Finally, this perovskite was introduced into a perovskite solar cell architecture, yielding an impressive power conversion efficiency for 2D perovskite (n = 5), approaching 10%. Further study of the device performance found that the losses in this device structure is mainly due to misalignment of the hole selective contact with the low-dimensional perovskite based on the hydroxyl barrier molecules. Contact angle and ambient air stability measurements provide information on the humidity tolerance of the perovskite that might change dramatically due to the substrate.

The barrier molecules were synthesized by reacting *meso*-1,4-diamino-2,3-butanediol dihydrochloride with an excess of HI to form a H-BuDAI_2 salt (hydroxylbutyldiammonium iodide; more details can be found in the experimental section). Single crystal X-ray diffraction (SC-XRD) measurement was performed on a single crystal of H-BuDAI_2 salt, where its structure is presented in Figure S1 in the Supporting Information (SI). The structure was reported at the Cambridge crystallographic data center, CCDC Number 2088432. The details of the structure can be found in Table S1. Films of

https://doi.org/10.1021/acsenergylett.1c01990
ACS Energy Lett. 2022, 7, 217−225

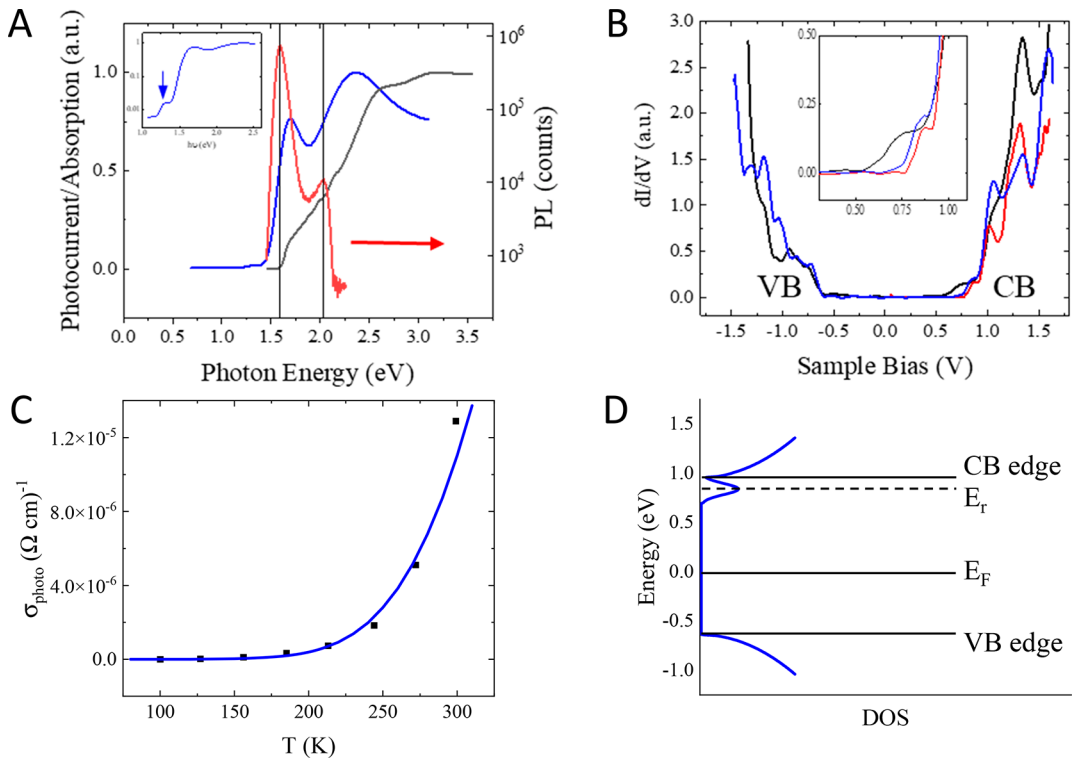

Figure 2. Electrical and optical properties of n = 5 layered perovskite films. (A) PL (red) absorption (black) and photocurrent (blue) spectra all depicting an energy gap of ∼1.6 eV and another energy level at about 2 eV. The absorption and photocurrent spectra are normalized each to its maximal value. Inset: Normalized photocurrent spectrum presented on logarithmic scale to better show the in-gap states. (B) Tunneling spectra measured at different locations along the sample, all showing a fundamental gap of ∼1.6 eV and in-gap states adjacent to the CB edge (the same dI/dV data are presented on a logarithmic scale in Figure S8). Inset: Blow-up focusing on the CB-edge region, showing the in-gap states. (C) Photoconductivity (σ_{photo}) as a function of temperature. The increase of σ_{photo} with temperature implies a recombination kinetics dominated by a shallow recombination level. Black dots: experimental results. Blue line: fit to the SRH model using the parameters extracted from the data presented in (A) and (B). (D) Band diagram as concluded from (A) and (B) and the SRH fit, where E_r is the recombination level energy.

low-dimensional perovskites were prepared using H-BuDAI$_2$, methylammonium iodide (MAI), and PbI$_2$ at a stoichiometric ratio according to the chemical formula (H-BuDA)-(MA)$_{n-1}$Pb$_n$I$_{3n+1}$, n = 1, 2, 4, and 5.

Figure 1A and Figures S2 and S3 present schematic illustrations of the barrier molecule attached to the inorganic perovskite sheets and the possible hydrogen bonds, which may be found in this structure.

Infrared (IR) vibrations for (H-BuDA)PbI$_4$ (n = 1) have been detected by polarization modulation infrared reflection absorption spectroscopy (PM-IRRAS) as shown in Figure 1B (the IR spectra of the precursors are available in Figure S4A). IR vibrations have been analyzed and measured before for MAPbI$_3$ perovskite.[21−24] Based on previous reports, the perovskite has several characteristic peaks in the range of 2900−3700 cm^{-1}. The aliphatic C−H stretch was detected at 2950−3080 cm^{-1}, while a much broader N−H stretch was detected at 3000−3200 cm^{-1} and correlated to the hydrogen bonded primary amine. Theoretical calculations[22,24] show that the ammonium group should have three vibrational modes. However, at room temperature, only the stronger vibrations, assigned for symmetric and asymmetric stretches, can be observed. In the case of the 2D perovskite, a broad intermolecular hydrogen bonded O−H stretch was detected at 3150−3400 cm^{-1}; this stretch of the alcohol group is indicative of hydrogen bonded OH species that is attached to the barrier chain. The O−H vibrational peak in the IR spectra of H-BuDAI$_2$ salt and 2,3-butandiol (Figure S4) was blue-shifted to higher wavenumbers. This shift can be associated with stronger interactions of the alcohol group of the barrier molecule with the perovskite structure.

The ammonium group is attached to a long organic chain, which increases the dipole moment on the N atom, thus inducing stronger IR signature. We further performed simulations that demonstrate the hydrogen bonds in the 2D perovskite structure (Figures S2 and S3). The simulations indicate that the intermolecular distance fits the formation of O−H···I and O−H···O−H hydrogen bonds. This structure suggests that N−H···I interactions in (H-BuDA)PbI$_4$ perovskite are expected to be partially replaced with the stronger interactions of O−H···I.[25] This hypothesis is also supported by the IR spectrum of 2D perovskite with butyldiammonium (BuDA) barrier (Figure S4C), which showed a red shift in the N−H vibration, correlated to formation of hydrogen bonds with the N−H group. These findings are correlated with the simulated structure that predicted the weaker N−H···I interactions will be the result of O−H···I interactions in the (H-BuDA)PbI$_4$ structure. The broad peak at ∼3400−3900 cm^{-1} was associated with water absorption on the perovskite surface. This peak appears typically during any measurement of perovskite in ambient air.[21] It can be summarized that the PM-IRRAS measurements provide indications for intermolecular hydrogen bonded O−H in the 2D perovskite while using H-BuDA as the barrier molecule.

https://doi.org/10.1021/acsenergylett.1c01990
ACS Energy Lett. 2022, 7, 217−225

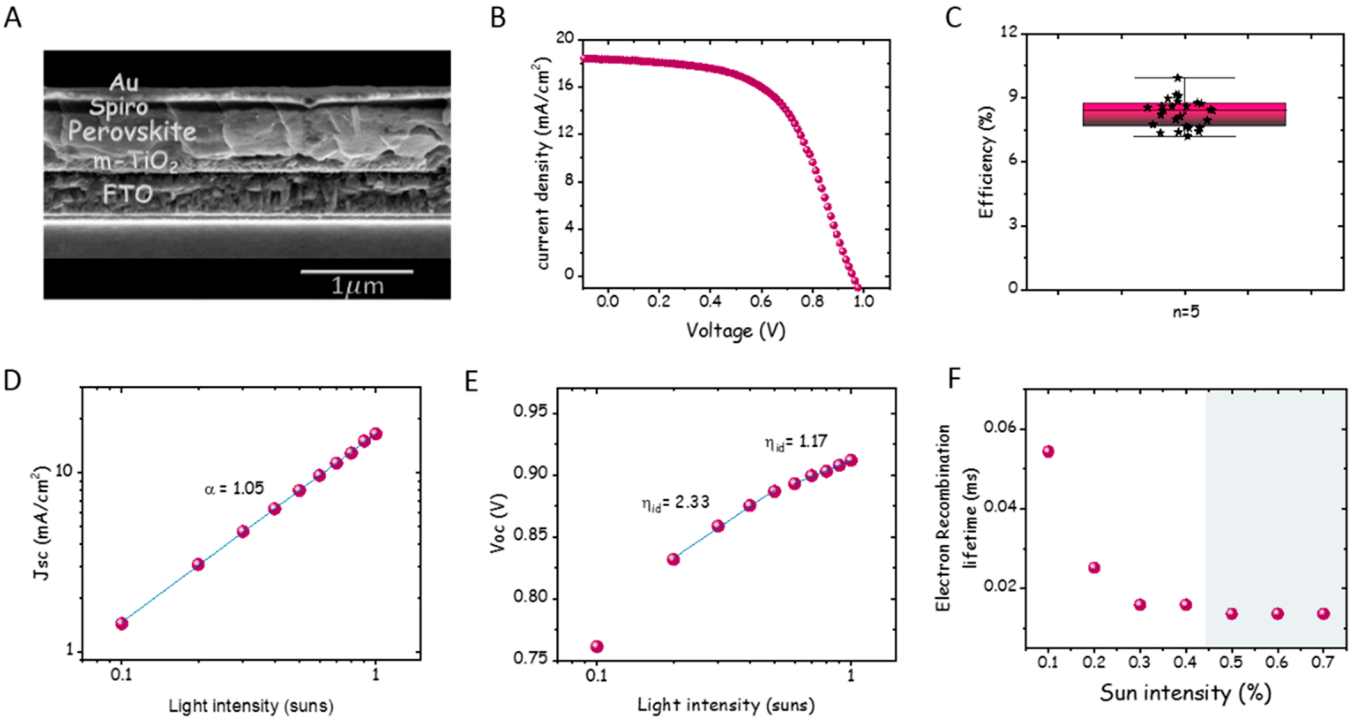

Figure 3. (A) SEM cross-section of the studied perovskite solar cell: FTO/m-TiO_2/n = 5 layered perovskite/Spiro/Au. Top view SEM and STM images can be observed in Figure S10. (B) J−V curve of the best performing device exceeding 9.9% PCE. (C) Efficiency statistics collected for devices containing one or two pixels each (total of 30 measured cells). The full statistic parameters (V_{oc}, J_{sc}, and FF) can be found in Figure S11. (D) and (E) Short circuit current and V_{oc} vs light intensities, respectably, showing α and ideality factors of the cell. J−V curves and PV parameters for different light intensities are shown in Figure S12. (F) Electron recombination lifetime in the solar cell at several light intensities (0.1−0.7 sun), extracted from intensity-modulated photovoltage spectroscopy (IMVS).

The change in the perovskite color with varying n value (Figure 1C) is in accord with the expected increase in the band gap with reducing the n value. This is further confirmed by the absorbance spectra (Figure 1E) that show similar characteristic curves to those reported previously for 2D perovskites.[11,12,15,26] The curves of n > 1 structures reveal also excitonic peaks of lower dimensionalities. This is further supported in the photoluminescence (PL) measurements (Figure S5A), which depict a blue shift with reducing n values. The XRD pattern (Figure 1D) of (H-BuDA)PbI_4 shows peaks at small (<∼14°) angles, which can be related to the dimensionality of the perovskite. The XRD pattern of (BuDA)PbI_4 perovskite (2D perovskite with butyl diammonium barrier[27]) is very similar to the XRD pattern of the (H-BuDA)PbI_4; therefore, it is possible to assign a similar configuration attachment of the barrier molecules except for the additional hydrogen bonds (see discussion in the SI and Figure S2). Both in the absorbance and XRD spectra additional features of other n values are observed for n = 2−5, which suggest that a mixture of low dimensional perovskites is present in these films.

Perovskite solar cells were fabricated, using mixed cations mixed halides perovskite, which demonstrate better PV performance than the traditional $MAPbI_3$ in 3D PSCs.[28,29] In this work we synthesized n = 5 perovskite, corresponding to (H-BuDA)$(Cs_{0.20}MA_{0.13}FA_{0.67})_4Pb_5(I_{0.9}Br_{0.1})_{16}$, serving as the absorber in our PSC (see below Figure 3A). Absorbance, PL, and XRD spectra of this perovskite can be observed in Figure S5. The absorbance spectrum shows a band edge at 780 nm and additional excitonic peaks at higher energies. The PL spectrum shows the main peak of the perovskite at 780 nm as well, and an additional small peak at 610 nm, which correlates with the absorbance excitonic peak of the low-dimensional perovskite. These features indicate the formation of lower n regions in the perovskite, as will be further discussed below. The measured PL lifetime is 88 ns (Figure S6A), similar to results of other lifetime measurements of perovskites.[13,15] This value is consistent also with the lifetime deduced from the mobility−lifetime product, $\mu\tau$, extracted from our photoconductivity measurements presented in Figure S6B, taking a reasonable mobility value of about 10 $cm^2/V{\cdot}s$.[30]

In order to further decipher the optoelectronic properties of these n = 5 perovskite films, we performed photocurrent spectroscopy and STS measurements and correlated the results with the optical absorbance and PL data. Figure 2A portrays PL and normalized optical absorbance spectra (here in eV units) together with a photoconductance spectrum measured on the same sample. The PL results are shown here on a logarithmic scale in order to emphasize the two peaks discussed above, at ∼1.6 and ∼2 eV. These PL data are further corroborated by the absorption spectrum that shows an onset at 1.6 eV, corresponding to the energy gap of the film, and a change in slope at ∼2 eV. Note that both these pure optical techniques did not reveal any evidence for the presence of electronic states within the energy gap of the film. The photoconductance spectrum confirms the optical results regarding the two band gaps, showing two photocurrent onsets close to 1.6 and 2 eV (but somewhat lower due to band-tailing). Note that in the latter technique the gaps are not determined by the peaks, which correspond instead to the onset of surface recombination. However, in contrast to the optical data, it clearly indicates also the presence of in-gap

https://doi.org/10.1021/acsenergylett.1c01990
ACS Energy Lett. 2022, 7, 217−225

states adjacent to the conduction-band (CB) onset, as seen at the inset of Figure 2A; the states are probably thermally coupled to the CB at room temperature.

To gain more information about these in-gap states as well as on the band structure of the film, we carried out local STS measurements, that are known to yield information on the local electronic density of states,[31] including on the energy gap and the position of the Fermi energy (relative to the band edges) and in-gap states in semiconductors.[32−34] Figure 2B presents typical $dI/dV-V$ tunneling spectra that were measured at different locations on the film. The spectra also indicate an energy gap of about 1.6 eV, in agreement with the above results. Moreover, they also show the presence of in-gap states close to the CB, as manifested by the small shoulders and peaks positioned at energies varying between 100 and 200 meV below the CB edge (see inset), in agreement with the photoconductance spectra. The tunneling spectra further show that the Fermi energy lies about 0.64 eV above the valence band (VB) edge, i.e., below the midgap, indicating that the film is a slightly p-type semiconductor.

Another important aspect that is related to the performance of a solar cell comprising such a film as the absorber is its photoconductivity properties. To study this, we measured the photoconductivity (σ_{photo}) as a function of temperature and illumination intensity and analyzed the results using the Shockley−Read−Hall (SRH) model.[30,35−37] More details regarding this model can be found in the Supporting Information.

Figure 2C shows the temperature dependence of the photoconductivity at an estimated photocarrier generation rate, G, of about 10^{20} cm^{-3} s^{-1} (see the SI). The increase of the photoconductivity with temperature indicates that the recombination kinetics in the film is governed by a shallow recombination level,[34,36] in agreement with the above STS and photoconductance spectra results, as corroborated by the fit to the SRH model presented in Figure 2C. Evidently, we could fit well the temperature dependence of the photoconductivity using parameters close to those extracted experimentally, namely, the energy gap, and the positions of the Fermi energy and the effective defect states energy relative to the VB edge, as follows: E_g = 1.6 eV, E_F = 0.64 eV, E_r = 1.48 eV (120 meV below the CB edge, in the range of the in-gap states found by STS). The hole (majority carrier) mobility is modeled as $\mu_p \propto \exp\left(-\frac{0.085}{k_BT}\right)$ where k_BT is in eV, as detailed in the Supporting Information (including Figure S7). We note that the good fits we obtained along with the good correspondence between our experimental results and the fitting parameters do not exclude the presence of other defects at other energies. However, they do suggest that the recombination kinetics is dominated by a shallow recombination level, as found by our STS and photocurrent spectroscopy results, and that we can describe the photoconductivity in this material by using such an effective level solely.

Mesoporous PSCs were fabricated following the architecture FTO/dense TiO_2/mesoporous TiO_2/n = 5 perovskite/Spiro-OMeTAD/gold, as illustrated in the cross-section scanning electron microscopy (SEM) image in Figure 3A. The power conversion efficiency (PCE) achieved by these devices is ca. 10%. Similar efficiencies for the n = 3−5 perovskite have been reported using a butylammonium spacer by the hot casting deposition method (planar substrates).[16,38,39] Higher PV results were achieved by using 2D/3D (n > 5) composition[13,15,40] or by using additives/solvents, which may increase the material dimensionality.[41−43] The current density vs voltage ($J-V$) curve of the best-performed device is presented in Figure 3B, demonstrating the open-circuit voltage (V_{oc}) of 0.96 V, the short circuit current density (J_{sc}) of 18.4 mA/cm^2, and 56% FF yielding 9.9% efficiency (the hysteresis loop of this device can be observed in Figure S9). While the J_{sc} value is satisfied for 1.6 eV energy gap, it can be seen that the cells suffer from a series resistance, which can be related to recombination in the selective contacts, mainly at the perovskite/hole transport layer (HTL) interface,[44,45] as will be discussed below. The top-view SEM image (Figure S10A) shows a uniform and pinhole-free surface that contains ∼80−100 nm perovskite grains. Figure S10B shows the STS image performed on the n = 5 perovskite, which displays a root-mean-square (RMS) roughness of about 10 nm. Statistical information about the PV performance of these devices is reported in Figure 3C and Figure S11.

To evaluate the device mechanism, the performance of the cells was recorded under increasing light intensities from 10 mW/cm^2 (0.1sun) to 100 mW/cm^2 (1 sun). In Figure S12B,C the plotted $J-V$ curves can be seen together with the specific PV parameters. $I-V$ curves of a perovskite film deposited onto a glass substrate under different light intensities can be found in the Supporting Information (Figure S11A). Increasing the light intensity results in the increase of the solar cells' efficiency, where the maximum performance is observed at ∼0.6 sun and stays stable for higher light intensity. The current density as a function of the light intensity on a logarithmic scale is presented in Figure 3D. The power-law dependency $J_{sc} \propto I^{\alpha}$ yields a slope of 1.05, which shows the proportional ratio between photon flux to current density. An α value close to 1 suggests that there is negligible space-charge recombination in the solar cell.[46,47] The V_{oc} as a function of the light intensity plotted on a semilogarithmic scale is shown in Figure 3E. This measurement provides a reliable method to determine the ideality factor, η_{id},[48,49] which lends information on the recombination mechanism in the solar cell and its origin.[46,48−51] The slope of this graph gives $\eta_{id}K_BTq^{-1}$, from which η_{id} can be extracted. Typically, η_{id} varies between 1 and 2, but higher values more than 5 were reported as well.[52] The curve presented in Figure 3E and Figure S12D displays two slopes, corresponding to two different ideality factors. In the case of low light intensity, ∼0.2−0.5 sun, a large value of n_{id} = 2.33 is calculated. This value indicates that the dominant losses mechanism is Shockley−Read−Hall (SRH) trap-assistant recombination in the depletion region, and intragap defect states. At higher illumination intensities, the slope deceased to 1.17. When η_{id} is close to 1, it may be interpreted incorrectly to conclude that the dominant losses are due to radiative recombination process; however, in the case of a perovskite film it is hard to believe that this is the main mechanism. Previous studies showed that in hole transport layer (HTL)-free perovskite solar cells the ideality factor is close to 1 or even lower than that, which is associated with surface recombination.[48,49] Considering these studies, a more general picture can be drawn, the perovskite exhibits bulk defect states that are dominant at low light intensities and responsible for the main recombination losses. At 50 mW/cm^2 or higher light intensities, these traps are already filled (or partially filled), and a free flow of carriers may occur. However, in this case, a new limitation appears, and the dominant recombination process is controlled by surface recombination. Intensity-modulated

https://doi.org/10.1021/acsenergylett.1c01990
ACS Energy Lett. 2022, 7, 217−225

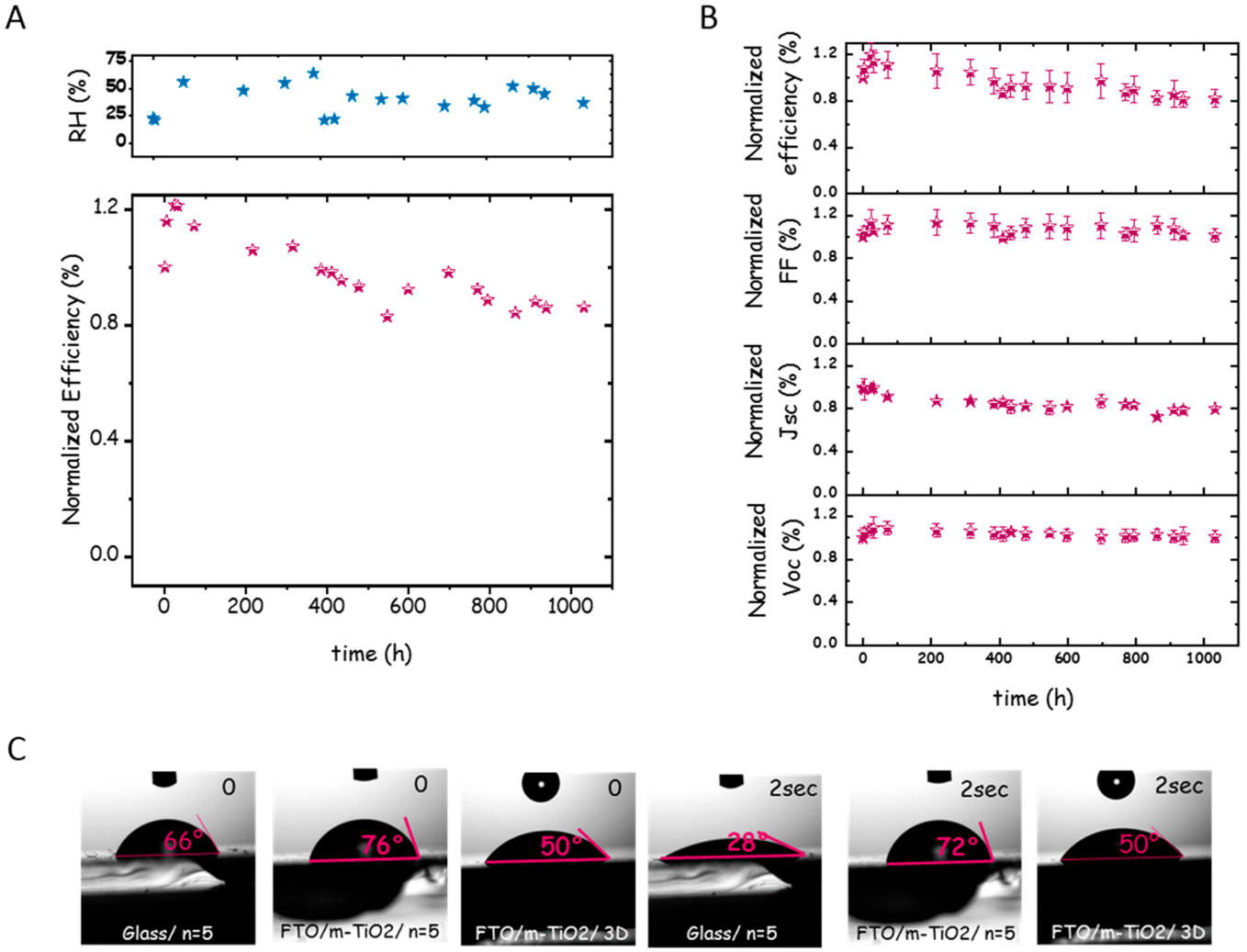

Figure 4. Stability test for non-encapsulate n = 5 perovskite solar cells performed at ambient air with relative humidity (RH) approaching 65%. (A) The efficiency of (H-BuDA)$(Cs_{0.20}MA_{0.13}FA_{0.67})_4Pb_5(I_{0.9}Br_{0.1})_{16}$ PSC over time, and the measured relative humidity at the same time of the PV measurement. After 1000 h the efficiency of the cells degraded to 82% of their initial efficiency. (B) The specific photovoltaics parameters (V_{oc}, J_{sc}, FF, and efficiency) of the cells over 1000 h (T_{80} = 1100 h). (C) The contact angle of FTO/m-TiO_2/n = 5 (H-BuDA)$(Cs_{0.20}MA_{0.13}FA_{0.67})_4Pb_5(I_{0.9}Br_{0.1})_{16}$ perovskite and the equivalent 3D film (FTO/m-TiO_2/$(Cs_{0.20}MA_{0.13}FA_{0.67})Pb(I_{0.9}Br_{0.1})_3$ showing more hydrophobic nature for the layered perovskite.

photovoltage spectroscopy (IMVS) measurements show the same trend around intensity of 0.5 sun. IMVS measurements provide information on the electron recombination lifetime of the cell under different light intensities.[15,53,54] Figure 3F and Figure S13B present the electron recombination lifetime in the perovskite measured by IMVS of the complete solar cell, where lifetimes of 10−60 μs for 10−70 mW/cm^2 illumination intensities were observed. As expected, increasing the light intensity results in a shorter lifetime. However, at intensities higher than ∼0.5 sun, the electron recombination lifetime is constant. In this range of illumination intensities, the surface recombination is dominant, suggesting that the limitation of the charge transfer at high illumination intensities is due to the selective contacts.

Charge extraction measurement[11,12] of the complete solar cells are depicted in Figure S13A, which shows that even after 20 s of the device being in the dark there are still charges that can be extracted. These results agree well with our previous finding regarding the high series resistance, which suggested that the resistivity is due to the selective contacts, mainly the perovksite/HTL interface. Figure S13C shows the electron recombination lifetime in the TiO_2 layer measured by IMVS. Here also, the lifetime is constant above a light intensity of ≥50 mW/cm^2. Therefore, we can conclude that the alignment of the energy levels of spiro-OMeTAD to the (H-BuDA)-$(Cs_{0.20}MA_{0.13}FA_{0.67})_4Pb_5(I_{0.9}Br_{0.1})_{16}$ perovskite is not optimal. These results suggest that the H-BuDA n = 5 perovskite has the potential to demonstrate an efficient solar cell, competitive with the traditional 3D PSCs, by better alignment of the perovskite's energy levels to the selective contacts.

Perovskite solar cells are known by their low stability in ambient air.[55−57] We tested the solar cell stability under ambient conditions, with an average relative humidity (RH) of about 50%. Figure 4A shows the stability of a nonencapsulated H-BuDA n = 5 perovskite solar cell over 1030 h and the measured humidity at the same time that the PV measurements were taken. The average PV parameters measured under 50% RH conditions are portrayed in Figure 4B. It can be seen that the cells preserved more than 80% of their initial efficiency over 1100 h. Moreover, after approximately three months

https://doi.org/10.1021/acsenergylett.1c01990
ACS Energy Lett. 2022, 7, 217−225

outside where the average humidity was about 57%, the cells still preserve 50% of their initial efficiency. Similar stability measurements (64% RH) for nonencapsulated 2D PSCs (n = 4) with a butylammonium barrier were reported.[16] These measurements showed almost complete degradation of the devices after ~25 h, which further support the improved stability of this new 2D perovskite structure.

Contact angle measurements performed on n = 5 H-BuDA perovskite further support the excellent stability under a humid environment. In this experiment, the angle between a water drop and the perovskite surface was measured for different samples.

The n = 5 H-BuDA perovskite and the equivalent 3D perovskite ($(Cs_{0.20}MA_{0.13}FA_{0.67})Pb(I_{0.9}Br_{0.1})_3$) were deposited on two different substrates, microscope glass substrate and FTO/m-TiO_2 substrate (Figure 4C and Figure S14). The contact angle between the water drop to n = 5 H-BuDA on the FTO/m-TiO_2 substrate was 76°, only slightly reducing during the entire time of measurement (1.5 min). Performing the same measurement on a 3D perovskite results in a 50° contact angle, manifesting the enhanced hydrophobic nature of the low-dimensional perovskite. Interestingly, the contact angle of n = 5 H-BuDA on a microscope glass substrate was 66° and the drop immediately started spreading over the surface, approaching a contact angle of 28° within only 2 s. This indicates that the n = 5 H-BuDA perovskite is arranged more effectively on the mesoporous TiO_2 substrate than on flat surfaces such as glass. The perovskite sheets are organized due to the affinity of the hydroxyl groups to the surface, similar to the carboxylic functional group.[19,20] The arrangement of the perovskite sheets on the surface is due to hydrogen bonds within the perovskite as discussed previously. It can be assumed that on a microscope glass substrate the perovskite is less organized; therefore, the hydroxyl groups are free to interact with water. The stability test and the contact angle measurements show that the tolerance of the n = 5 HBuDA perovskite to humidity is very high comparing to other 2D and 3D organic−inorganic perovskite structures.

This work demonstrates the use of a new spacer molecule comprising hydroxyl functional groups in low-dimensional perovskite that form hydrogen bonding to the iodide and in between the OH groups. Optical measurements and polarization modulation infrared reflection absorption spectroscopy show the structural properties of this new 2D perovskite. The low-dimensional HBuDA perovskite provides a stable structure and efficient organization of the perovskite sheets on top of mesoporous TiO_2 substrate. As a result, a power conversion efficiency of 10% was observed for n = 5 solar cells. Photocurrent spectroscopy and scanning tunneling spectroscopy measurements reveal the band structure of this low-dimensional perovskite with in-gap states close to the CB edge. The operation mechanism of this solar cell was further evaluated by the light intensity dependence on the PV parameters, suggesting that the limitation of the charge transfer at high illumination intensities is due to the interface of the perovskite with the hole selective contact. Stability measurements show that the cells retain their efficiency over 1030 h under relative humidity of more than 50%. This work presents a unique spacer molecule that opens the way for high efficiency and stable 2D perovskite solar cells.

■ ASSOCIATED CONTENT

Supporting Information

The Supporting Information is available free of charge at https://pubs.acs.org/doi/10.1021/acsenergylett.1c01990.

$H\text{-}BuDAI_2$ single crystal data, $(H\text{-}BuDA)PbI_4$ structure simulation, hydrogen bond discussion, IR spectra for 2D perovskite and its precursors, PL, PL decay, absorbance, powder XRD, mobility lifetime, Shockley−Read−Hall model, hysteresis, surface morphology, statistics, *IV* curves under various light intensities, charge extraction, IMVS, contact angle, and experimental details (PDF)

■ AUTHOR INFORMATION

Corresponding Author

Lioz Etgar − *Institute of Chemistry, Casali Center for Applied Chemistry and the Center for Nanoscience and Nanotechnology, The Hebrew University of Jerusalem, Jerusalem 91904, Israel;* orcid.org/0000-0001-6158-8520; Email: lioz.etgar@mail.huji.ac.il

Authors

Bat-El Cohen − *Institute of Chemistry, Casali Center for Applied Chemistry and the Center for Nanoscience and Nanotechnology, The Hebrew University of Jerusalem, Jerusalem 91904, Israel*

Tal Binyamin − *Institute of Chemistry, Casali Center for Applied Chemistry and the Center for Nanoscience and Nanotechnology, The Hebrew University of Jerusalem, Jerusalem 91904, Israel*

Tzipora Ben-Tzvi − *Institute of Chemistry and the Center for Nanoscience and Nanotechnology, The Hebrew University of Jerusalem, Jerusalem 91904, Israel*

Oren Goldberg − *Racah Institute of Physics, The Hebrew University of Jerusalem, Jerusalem 91904, Israel*

Adi Schlesinger − *Azrieli, Jerusalem College of Engineering, Jerusalem 91904, Israel*

Isaac Balberg − *Racah Institute of Physics, The Hebrew University of Jerusalem, Jerusalem 91904, Israel;* orcid.org/0000-0002-0664-8735

Oded Millo − *Racah Institute of Physics, The Hebrew University of Jerusalem, Jerusalem 91904, Israel;* orcid.org/0000-0003-4377-0294

Elad Gross − *Institute of Chemistry and the Center for Nanoscience and Nanotechnology, The Hebrew University of Jerusalem, Jerusalem 91904, Israel;* orcid.org/0000-0002-8330-7299

Doron Azulay − *Racah Institute of Physics, The Hebrew University of Jerusalem, Jerusalem 91904, Israel; Azrieli, Jerusalem College of Engineering, Jerusalem 91904, Israel*

Complete contact information is available at: https://pubs.acs.org/10.1021/acsenergylett.1c01990

Notes

The authors declare no competing financial interest.

■ ACKNOWLEDGMENTS

L.E. acknowledge the support by the AFRL award and ISF grant number 937/18. B.E.C thanks the ministry of energy for their financial support. O.M. thanks the partial support of the ISF grant 661/16. O.M. thanks support from the Harry de Jur Chair in Applied Science. D.A. thanks the support of the

Azrieli college research Fund. Thank to Dr. Benny Bogoslavsky who performed the SCXRD and the simulations.

REFERENCES

(1) Goldschmidt, V. M. Die gesetze der krystallochemie. *Naturwissenschaften* **1926**, *14*, 477−485.
(2) Mitzi, D. B.; Feild, C. A.; Harrison, W. T. A.; Guloy, A. M. Conducting tin halides with a layered organic-based perovskite structure. *Nature* **1994**, *369*, 467−469.
(3) Saparov, B.; Mitzi, D. B. Organic-Inorganic Perovskites: Structural Versatility for Functional Materials Design. *Chem. Rev.* **2016**, *116*, 4558−4596.
(4) Li, X.; Hoffman, J. M.; Kanatzidis, M. G. The 2D halide perovskite rulebook: How the spacer influences everything from the structure to optoelectronic device efficiency. *Chem. Rev.* **2021**, *121*, 2230−2291.
(5) Misra, R. K.; Cohen, B. A.-E.; Etgar, L. Low-Dimensional Organic-Inorganic Halide Perovskite: Structure, Properties, and Applications. *ChemSusChem* **2017**, *10*, 3712.
(6) Kim, E.-B.; Akhtar, M. S.; Shin, H.-S.; Ameen, S.; Nazeeruddin, M. K. A review on two-dimensional (2D) and 2D-3D multidimensional perovskite solar cells: Perovskites structures, stability, and photovoltaic performances. *J. Photochem. Photobiol., C* **2021**, *48*, 100405.
(7) Ishihara, T.; Hong, X.; Ding, J.; Nurmikko, A. V. Dielectric confinement effect for exciton and biexciton states in PbI4-based two-dimensional semiconductor structures. *Surf. Sci.* **1992**, *267*, 323−326.
(8) Ishihara, T. Optical properties of PbI-based perovskite structures. *J. Lumin.* **1994**, *60*−*61*, 269−274.
(9) Mitzi, D. B. Solution-processed inorganic semiconductors. *J. Mater. Chem.* **2004**, *14*, 2355−2365.
(10) Quan, L. N.; et al. Ligand-Stabilized Reduced-Dimensionality Perovskites. *J. Am. Chem. Soc.* **2016**, *138*, 2649−2655.
(11) Cohen, B. El; Wierzbowska, M.; Etgar, L. High efficiency quasi 2D lead bromide perovskite solar cells using various barrier molecules. *Sustain. Energy Fuels* **2017**, *1*, 1935.
(12) Cohen, B.-E.; Wierzbowska, M.; Etgar, L. High Efficiency and High Open Circuit Voltage in Quasi 2D Perovskite Based Solar Cells. *Adv. Funct. Mater.* **2017**, *27*, 1604733.
(13) Lee, J. W.; et al. 2D perovskite stabilized phase-pure formamidinium perovskite solar cells. *Nat. Commun.* **2018**, *9*, 3021.
(14) Cao, D. H.; Stoumpos, C. C.; Farha, O. K.; Hupp, J. T.; Kanatzidis, M. G. 2D Homologous Perovskites as Light-Absorbing Materials for Solar Cell Applications. *J. Am. Chem. Soc.* **2015**, *137*, 7843−7850.
(15) Cohen, B. El; Li, Y.; Meng, Q.; Etgar, L. Dion-Jacobson Two-Dimensional Perovskite Solar Cells Based on Benzene Dimethanammonium Cation. *Nano Lett.* **2019**, *19*, 2588−2597.
(16) Tsai, H.; et al. High-efficiency two-dimensional ruddlesden-popper perovskite solar cells. *Nature* **2016**, *536*, 312−317.
(17) Steiner, T. The Hydrogen Bond in the Solid State. *Angew. Chem., Int. Ed.* **2002**, *41*, 48−76.
(18) Berg, Jeremy M.; Tymoczko, John L.; Stryer, L. *Biochemistry*, 5th ed.; Freeman, 2002.
(19) Zhu, L. F.; et al. Efficient perovskite solar cells via simple interfacial modification toward a mesoporous TiO2 electron transportation layer. *RSC Adv.* **2016**, *6*, 82282−82288.
(20) Cao, J.; et al. Thiols as interfacial modifiers to enhance the performance and stability of perovskite solar cells. *Nanoscale* **2015**, *7*, 9443−9447.
(21) Müller, C.; et al. Water Infiltration in Methylammonium Lead Iodide Perovskite: Fast and Inconspicuous. *Chem. Mater.* **2015**, *27*, 7835−7841.
(22) Brivio, F.; et al. Lattice dynamics and vibrational spectra of the orthorhombic, tetragonal, and cubic phases of methylammonium lead iodide. *Phys. Rev. B: Condens. Matter Mater. Phys.* **2015**, *92*, 144308.
(23) Glaser, T.; et al. Infrared Spectroscopic Study of Vibrational Modes in Methylammonium Lead Halide Perovskites. *J. Phys. Chem. Lett.* **2015**, *6*, 2913−2918.
(24) Pérez-Osorio, M. A.; et al. Vibrational Properties of the Organic-Inorganic Halide Perovskite CH3NH3PbI3 from Theory and Experiment: Factor Group Analysis, First-Principles Calculations, and Low-Temperature Infrared Spectra. *J. Phys. Chem. C* **2015**, *119*, 25703−25718.
(25) Steiner, T. Hydrogen-Bond Distances to Halide Ions in Organic and Organometallic Crystal Structures: Up-to-date Database Study. *Acta Crystallogr., Sect. B: Struct. Sci.* **1998**, *54*, 456−463.
(26) Xing, J.; et al. Color-stable highly luminescent sky-blue perovskite light-emitting diodes. *Nat. Commun.* **2018**, *9*, 3541.
(27) Li, X.; et al. Two-Dimensional Halide Perovskites Incorporating Straight Chain Symmetric Diammonium Ions, (NH3CmH2 mNH3)-(CH3NH3)n-1PbnI3 n+1 (m = 4−9; N = 1−4). *J. Am. Chem. Soc.* **2018**, *140*, 12226−12238.
(28) Saliba, M.; et al. Cesium-containing triple cation perovskite solar cells: Improved stability, reproducibility and high efficiency. *Energy Environ. Sci.* **2016**, *9*, 1989−1997.
(29) Saliba, M.; et al. How to Make over 20% Efficient Perovskite Solar Cells in Regular (n-i-p) and Inverted (p-i-n) Architectures. *Chem. Mater.* **2018**, *30*, 4193−4201.
(30) Levine, I.; et al. Mobility-Lifetime Products in MAPbI3 Films. *J. Phys. Chem. Lett.* **2016**, *7*, 5219−5226.
(31) Weissendanger, R. *Scanning Probe Microscopy and Spectroscopy: Methods and Applications*; Cambridge University Press, 1994.
(32) Azulay, D.; Balberg, I.; Chu, V.; Conde, J. P.; Millo, O. Current routes in hydrogenated microcrystalline silicon. *Phys. Rev. B: Condens. Matter Mater. Phys.* **2005**, *71*, 113304.
(33) Ashkenazi, O.; et al. Size-dependent donor and acceptor states in codoped Si nanocrystals studied by scanning tunneling spectroscopy. *Nanoscale* **2017**, *9*, 17884−17892.
(34) Azulay, D.; et al. On the influence of multiple cations on the in-gap states and phototransport properties of iodide-based halide perovskites. *Phys. Chem. Chem. Phys.* **2018**, *20*, 24444−24452.
(35) Bube, R. H. *Photoelectronic Properties of Semiconductors*; Cambridge University Press, 1992.
(36) Zakay, N.; et al. Phototransport properties of CuInSe2 thin films: The influence of na and planar defects. *Phys. Rev. Appl.* **2020**, *14*, 024005.
(37) Balberg, I.; Dover, Y.; Savir, E.; Von Huth, P. Basic physics of phototransport as manifested in thin films of In-doped CdTe. *Phys. Rev. B: Condens. Matter Mater. Phys.* **2010**, *82*, 205302.
(38) Blancon, J. C.; et al. Extremely efficient internal exciton dissociation through edge states in layered 2D perovskites. *Science (Washington, DC, U. S.)* **2017**, *355*, 1288−1292.
(39) Soe, C. M. M.; et al. Understanding Film Formation Morphology and Orientation in High Member 2D Ruddlesden−Popper Perovskites for High-Efficiency Solar Cells. *Adv. Energy Mater.* **2018**, *8*, 1700979.
(40) Li, P. Phase Pure 2D Perovskite for High-Performance 2D−3D Heterostructured Perovskite Solar Cells. *Adv. Mater.* **2018**, *30*, 1805323.
(41) Ren, H.; et al. Efficient and stable Ruddlesden−Popper perovskite solar cell with tailored interlayer molecular interaction. *Nat. Photonics* **2020**, *14*, 154−163.
(42) Luo, T.; et al. Compositional Control in 2D Perovskites with Alternating Cations in the Interlayer Space for Photovoltaics with Efficiency over 18%. *Adv. Mater.* **2019**, *31*, 1903848.
(43) Zheng, Y.; et al. Oriented and Uniform Distribution of Dion−Jacobson Phase Perovskites Controlled by Quantum Well Barrier Thickness. *Sol. RRL* **2019**, *3*, 1900090.
(44) Juarez-Perez, E. J.; et al. Role of the selective contacts in the performance of lead halide perovskite solar cells. *J. Phys. Chem. Lett.* **2014**, *5*, 680−685.
(45) Mundhaas, N.; et al. Series Resistance Measurements of Perovskite Solar Cells Using Jsc−Voc Measurements. *Sol. RRL* **2019**, *3*, 1800378.
(46) Singh, T.; Miyasaka, T. Stabilizing the Efficiency Beyond 20% with a Mixed Cation Perovskite Solar Cell Fabricated in Ambient Air under Controlled Humidity. *Adv. Energy Mater.* **2018**, *8*, 1700677.

https://doi.org/10.1021/acsenergylett.1c01990
ACS Energy Lett. 2022, 7, 217−225

(47) Mihailetchi, V. D.; Wildeman, J.; Blom, P. W. M. Space-charge limited photocurrent. *Phys. Rev. Lett.* **2005**, DOI: 10.1103/PhysRevLett.94.126602.
(48) Tress, W.; et al. Interpretation and evolution of open-circuit voltage, recombination, ideality factor and subgap defect states during reversible light-soaking and irreversible degradation of perovskite solar cells. *Energy Environ. Sci.* **2018**, *11*, 151−165.
(49) Wolff, C. M.; Caprioglio, P.; Stolterfoht, M.; Neher, D. Nonradiative Recombination in Perovskite Solar Cells: The Role of Interfaces. *Adv. Mater.* **2019**, *31*, 1902762.
(50) Caprioglio, P.; et al. On the Origin of the Ideality Factor in Perovskite Solar Cells. *Adv. Energy Mater.* **2020**, *10*, 2000502.
(51) Courtier, N. E. Interpreting ideality factors for planar perovskite solar cells: Ectypal diode theory for steady-state operation. *Phys. Rev. Appl.* **2020**, *14*, 024031.
(52) Pockett, A.; et al. Characterization of planar lead halide perovskite solar cells by impedance spectroscopy, open-circuit photovoltage decay, and intensity-modulated photovoltage/photocurrent spectroscopy. *J. Phys. Chem. C* **2015**, *119*, 3456−3465.
(53) Bou, A.; et al. Beyond Impedance Spectroscopy of Perovskite Solar Cells: Insights from the Spectral Correlation of the Electro-optical Frequency Techniques. *J. Phys. Chem. Lett.* **2020**, *11*, 8654−8659.
(54) Wang, F.; Chen, Y.; Han, G.; Zhang, Q.; Ma, Q. The interface and its role in carrier transfer/recombination dynamics for the planar perovskite solar cells prepared under fully open air conditions. *Curr. Appl. Phys.* **2016**, *16*, 1353−1363.
(55) Song, Z.; et al. Perovskite Solar Cell Stability in Humid Air: Partially Reversible Phase Transitions in the PbI2-CH3NH3I-H2O System. *Adv. Energy Mater.* **2016**, *6*, 1600846.
(56) Khenkin, M. V.; et al. Consensus statement for stability assessment and reporting for perovskite photovoltaics based on ISOS procedures. *Nat. Energy* **2020**, *5*, 35−49.
(57) Wang, R. A Review of Perovskites Solar Cell Stability. *Adv. Funct. Mater.* **2019**, *29*, 1808843.

https://doi.org/10.1021/acsenergylett.1c01990
ACS Energy Lett. 2022, 7, 217−225